Detecting and locating light atoms from high-resolution STEM images : the quest for a single optimal design

Detecting and locating light atoms from high-resolution STEM images: The quest for a single optimal design

J. Gonnissen, A. De Backer, A.J. den Dekker, J. Sijbers, S. Van Aert

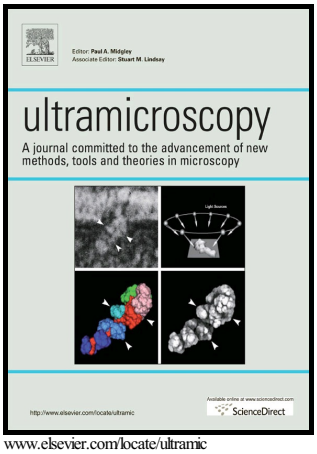

www.elsevier.com/locate/ultramic

PII: S0304-3991(16)30112-7
DOI: http://dx.doi.org/10.1016/j.ultramic.2016.07.014
Reference: ULTRAM12176

To appear in: *Ultramicroscopy*

Received date: 22 April 2016
Revised date: 28 June 2016
Accepted date: 22 July 2016

Cite this article as: J. Gonnissen, A. De Backer, A.J. den Dekker, J. Sijbers and S. Van Aert, Detecting and locating light atoms from high-resolution STEM images: The quest for a single optimal design, *Ultramicroscopy*, http://dx.doi.org/10.1016/j.ultramic.2016.07.014

Detecting and locating light atoms from high-resolution STEM images: the quest for a single optimal design

J. Gonnissen[a], A. De Backer[a], A.J. den Dekker[b,c], J. Sijbers[b], S. Van Aert[a,*]

[a]*Electron Microscopy for Materials Science (EMAT), University of Antwerp, Groenenborgerlaan 171, B-2020 Antwerp, Belgium*
[b]*iMinds-Vision Lab, University of Antwerp, Universiteitsplein 1, 2610 Wilrijk, Belgium*
[c]*Delft Center for Systems and Control (DCSC), Delft University of Technology, Mekelweg 2, 2628 CD Delft, The Netherlands*

Abstract

In the present paper, the optimal detector design is investigated for both detecting and locating light atoms from high resolution scanning transmission electron microscopy (HR STEM) images. The principles of detection theory are used to quantify the probability of error for the detection of light atoms from HR STEM images. To determine the optimal experiment design for locating light atoms, use is made of the so-called Cramér-Rao Lower Bound (CRLB). It is investigated if a single optimal design can be found for both the detection and location problem of light atoms. Furthermore, the incoming electron dose is optimised for both research goals and it is shown that picometre range precision is feasible for the estimation of the atom positions when using an appropriate incoming electron dose under the optimal detector settings to detect light atoms.

Keywords: High-resolution scanning transmission electron microscopy (HR STEM), Electron microscope design and characterisation, Data processing/image processing

1. Introduction

In the past few years, a lot of research has been done to improve the imaging power to detect light atoms like oxygen, lithium, and hydrogen, since they play a key-role in a range of industrial applications such as lithium-batteries or hydrogen-storage materials. Since material properties are crucially dependent on the exact atomic arrangement, an estimation of the atomic column positions with picometre range precision is needed [1–3].
The performance of a STEM experiment is often evaluated qualitatively, which means in terms of direct visual interpretability. For this purpose, the image contrast and signal-to-noise ratio (SNR) are useful criteria. However, in the past few years, electron microscopy has evolved toward a quantitative technique, aiming at accurate and precise numbers for the parameters of interest. If images are interpreted quantitatively, the principles of statistical parameter estimation theory and statistical detection theory enable one to quantify the attainable precision with which atoms can be located and the probability of error to detect atom columns [1, 4–8]. The experiment design for which the precision and/or probability of error is optimal does not necessaraly correspond to the experimental settings leading to the highest SNR or the best image contrast. If one interprets the STEM images quantitatively, reliable quantitative structure information can be retrieved using (high angle) annular dark field ((HA)ADF) STEM [9–21]. Recently, advances have been made in the design of new detectors. The use of pixelated detectors enables a high flexibility in the choice of detector settings [22–24]. In this work, a quantitative analysis will be performed to investigate where in the detector plane the most sensitive region is located for both detecting and locating light atoms, which can help experimentalists when choosing the appropriate camera length for their experiment. The ultimate goal is then to obtain quantitatively the optimal experiment design for which the unknown structure parameters are obtained with the highest possible precision. In this work, the inner and outer STEM detector angles are optimised. An appropriate theoretical tool using statistical detection theory [25] to derive this optimal experiment design in terms of detecting light atoms was proposed in [26]. The so-called probability of error

*Corresponding author
Email address: sandra.vanaert@uantwerpen.be (S. Van Aert)
[1]*Phone*: +32 3 2653252

can be derived as a function of the experiment design when comparing two or more hypotheses, where every hypothesis corresponds to the presence or absence of a specific atom type, for which a binary or multiple hypothesis test can be performed. For the computation of this probability of error, realistic simulations describing the experimental images can be used [19, 27–31] together with knowledge about the statistics of the image pixel values. The experimental settings leading to the lowest probability to decide the wrong hypothesis then correspond to the optimal experiment design.
One can not only investigate the optimal detector design in order to detect light atoms, but also derive the optimal detector settings to optimise the precision with which the atomic column positions can be estimated. The attainable precision with which unknown continuous structure parameters can be estimated, can be obtained using the concept of Fisher information. The ultimate precision is given by the lowest possible variance with which an unknown parameter can be estimated from a set of observations of which the probability distribution function is assumed to be known [32–34]. An expression for this lower bound on the variance with which the atomic column positions can be estimated from HR STEM images can be determined and is given by the so-called Cramér-Rao Lower Bound (CRLB) [1, 33–36]. Since the CRLB is independent of the used estimation method, it gives the intrinsic limit to the precision that can be obtained. This lower bound is a function of the microscope settings, of which at least some are adjustable, like the annular STEM detector and probe settings. The optimal statistical experiment design of a HR STEM experiment for locating light atoms is then given by the microscope settings that minimise the CRLB [37, 38].

The goal in this work is to investigate if both detecting and locating light atoms with the highest possible precision would lead to the same optimal experiment design. To illustrate the concept, the problem of suggesting optimal detector settings to detect the oxygen positions in $SrTiO_3$ is considered, as well as detecting the lithium atoms in LiV_2O_4. Therefore, a binary hypothesis test is performed where both hypotheses correspond to either the presence or absence of the oxygen or lithium atoms in the crystal. After optimal experiment designs have been obtained for the detection of the oxygen and lithium columns, a detailed simulation study is performed for the same crystals $SrTiO_3$ and LiV_2O_4, where the question is for which detector design the oxygen and lithium columns can be located from HR STEM images with the ultimate precision. Furthermore, both research questions are investigated as a function of the incoming electron dose. This allows one to investigate which electron dose is ultimately required to detect and locate light atoms with sufficient statistical significance.

The paper is organised as follows: the probability function of the observations, which is needed to calculate the probability of error and the CRLB, is introduced in Section 2. In Section 3, the procedure to optimise the experiment design is explained and discussed, using both the probability of error and the CRLB as optimality criteria. The results for the optimal experiment design are given in Section 4 for the detection of light atomic columns, and in Section 5 for locating the atoms. In Section 6, the results are discussed and in Section 7 conclusions are drawn.

2. The probability function of the observations

Every STEM experiment will contain certain inherent fluctuations. Therefore, different sets of STEM observations will always slightly differ, although they are made under the same imaging conditions. To describe this stochastic behaviour, we can model the observations as stochastic variables, which are defined by their probability (density) function (P(D)F) [34]. When assuming that the STEM observations are statistically independent electron counting results, this PF can be accurately modelled as a Poisson distribution. Consider a set of NM observations $\{w_{nm}|n = 1, ..., N; m = 1, ..., M\}$, where the index nm corresponds to the probe at position $(x_n, y_m)^T$. The probability that the observation w_{nm} is equal to ω_{nm} is given by [39]:

$$\frac{\lambda_{nm}^{\omega_{nm}}}{\omega_{nm}!} \exp\left(-\lambda_{nm}\right), \tag{1}$$

where the parameter $\lambda_{nm} = I_{nm} \cdot D \cdot \Delta x \Delta y$ corresponds to the expectation values of the pixel intensities of the STEM image, with D the incoming electron dose per unit area, $\Delta x \Delta y$ the pixel area, and I_{nm} the expected fraction of incoming electrons detected at the corresponding probe position. In general, these expectation models can be computed using prior knowledge of a given input material's structure and a given set of microscope parameters with software that allows one to simulate STEM images. In this work, use will be made of the STEMsim software developed by A. Rosenauer [28]. Since the pixel values in a STEM image are assumed to be statistically independent, the probability that a set of observations $\boldsymbol{w} = (w_{11}...w_{NM})^T$ is equal to $\boldsymbol{\omega} = (\omega_{11}...\omega_{NM})^T$ is equal to the product of all probabilities given by Eq.

(1):

$$p_{\mathbf{w}}(\omega) = \prod_{n=1}^{N}\prod_{m=1}^{M} \frac{\lambda_{nm}^{\omega_{nm}}}{\omega_{nm}!} \exp\left(-\lambda_{nm}\right). \tag{2}$$

3. Optimal experiment design

3.1. Statistical detection theory: detecting atoms

When one is considering the problem of detecting light atoms from HR STEM images, the question is if a specific atom is present or absent in the STEM image. This can be translated into a binary hypothesis test of which the hypotheses are given by:

$$\begin{aligned} \mathcal{H}_0 &: \mathrm{Z} = \mathrm{Z}_1 \\ \mathcal{H}_1 &: \mathrm{Z} \in \emptyset \end{aligned} \tag{3}$$

where $\mathcal{H}_0$ is referred to as the null hypothesis, in which the atomic number Z equals a specific value Z_1, and $\mathcal{H}_1$ as the alternative hypothesis describing the absence of an atom of any type. The theory for binary hypothesis testing is derived in [26] for the detection of light atoms and for readability of this work, this theoretical background is presented in Appendix A. In [26], it is shown that the probability of deciding the wrong hypothesis, i.e. the probability of error, is approximately given by:

$$\mathrm{P_e} = \frac{1}{2}\left[\Phi\left(\frac{-\mu_{\mathcal{H}_1}}{\sigma_{\mathcal{H}_1}}\right) + \Phi\left(\frac{\mu_{\mathcal{H}_0}}{\sigma_{\mathcal{H}_0}}\right)\right] \tag{4}$$

with

$$\mu_{\mathcal{H}_i} = \sum_{n=1}^{N}\sum_{m=1}^{M} \lambda_{\mathcal{H}_i,nm} \ln\frac{\lambda_{\mathcal{H}_1,nm}}{\lambda_{\mathcal{H}_0,nm}} - \lambda_{\mathcal{H}_1,nm} + \lambda_{\mathcal{H}_0,nm}, \tag{5}$$

$$\sigma_{\mathcal{H}_i}{}^2 = \sum_{n=1}^{N}\sum_{m=1}^{M} \lambda_{\mathcal{H}_i,nm}\left(\ln\frac{\lambda_{\mathcal{H}_1,nm}}{\lambda_{\mathcal{H}_0,nm}}\right)^2. \tag{6}$$

In the expression for $\mathrm{P_e}$, $\Phi(.)$ is the cumulative distribution function of the standard normal distribution, $\mu_{\mathcal{H}_i}$ the expected value and $\sigma_{\mathcal{H}_i}$ the standard deviation.

3.2. The Cramér-Rao Lower Bound: attainable precision for locating atoms

The goal in experiment design is to find the experimental settings that achieve the ultimate precision from a given set of observations. If one now wants to determine the position of a certain atomic column from a HR STEM image with the highest possible precision, the concept of Fisher information has to be used instead of detection theory. Using this concept, the most sensitive region of the detector can be found, as well as the precise optimal inner and outer detector angles, by investigating the CRLB as a function of the detector design. Since the theory of the CRLB is already well clarified in previous work [33–36], only the expression used in this paper for locating light atomic columns is given here. A detailed derivation of the CRLB is presented in Appendix B.

The CRLB has already been evaluated for locating atomic columns by Van Aert et al. [1]. However, in that study only a simple channeling model was considered for the STEM images which did not include thermal diffuse scattering. In this work, a more realistic simulation study is performed. In Section 6, it will be discussed if the same optimal experiment design is obtained based on these realistic simulations, in comparison with the results found in [1]. The observable random variable $\boldsymbol{w}$ carries information about an unknown parameter, which in this case is the position parameter vector $\boldsymbol{\Theta}$. It is proven that for the class of unbiased estimators $\widehat{\boldsymbol{\Theta}}$, the ultimate precision is given by a lower bound on their variance, the CRLB:

$$\mathrm{var}(\widehat{\Theta}_r) \geq \left[F^{-1}\right]_{rr}, \tag{7}$$

where $r \in \{1, ..., R\}$ with R the number of components of $\widehat{\boldsymbol{\Theta}}$ and $[F^{-1}]_{rr}$ the rth diagonal element of the inverse of the Fisher information matrix. In this sense, F^{-1} represents a lower bound on the variances of all unbiased estimators. The matrix F^{-1} is the CRLB on the variance of $\widehat{\boldsymbol{\Theta}}$. If we consider the position parameter vector $\boldsymbol{\Theta}$ and the joint Poisson probability function for the pixel intensities in a STEM image given by Eq. (2), it can be shown that the elements of the Fisher information matrix are given by [1]:

$$F_{rs} = \sum_{n=1}^{N}\sum_{m=1}^{M} \frac{1}{\lambda_{nm}} \frac{\partial\lambda_{nm}}{\partial\Theta_r}\frac{\partial\lambda_{nm}}{\partial\Theta_s}, \tag{8}$$

with $\lambda_{nm} = I_{nm} \cdot D \cdot \Delta x \Delta y$, the expectation values of the pixel intensities of the STEM image. For the estimation of the position of a single atomic column, the position parameter vector equals $\boldsymbol{\Theta} = (\Theta_x, \Theta_y)$. Suppose that $\widehat{\boldsymbol{\Theta}}$ is an unbiased estimator of $\boldsymbol{\Theta}$. The CRLB is then the 2-by-2 covariance matrix F^{-1} whose diagonal elements define lower bounds on the variances of the elements of $\widehat{\boldsymbol{\Theta}}$. The precision with which the atom column coordinates can be measured is therefore represented by the diagonal elements of the CRLB. Note that the CRLB is only defined for continuous parameters, such as the atomic column position, and can be calculated as a function of different experimental settings. Therefore, it is

an excellent tool to optimise the annular STEM detector in order to achieve the ultimate precision for locating light atomic columns, but it cannot be defined for the detection problem since the absence or presence of an atomic type is not a continuous parameter.

3.3. Practical implementation

As already mentioned before, one can not only investigate the optimal detector settings to detect light elements, but also optimise the experiment design in order to determine the position of the light atomic columns with the highest possible precision. Therefore, the CRLB introduced in Section 3.2, was computed as a function of the inner and outer detector collection angles for the position of the central oxygen column in the crystal $SrTiO_3$ as well as for the position of the central lithium column in the crystal LiV_2O_4. This has been investigated for the commonly used semi-convergence angles of 20 mrad for $SrTiO_3$ and 21.7 mrad for LiV_2O_4, and for different crystal thicknesses, up to 30 nm thick (i.e. a column of 75 atoms) in the case of $SrTiO_3$, and up to 4.66 nm thick (i.e. a column of 8 atoms) in the case of LiV_2O_4. To calculate the partial derivatives in the expression for the Fisher information matrix, given by Eq. (8), different STEM images for the $SrTiO_3$ and LiV_2O_4 crystals are simulated, where the central oxygen or lithium column in the field of view is shifted both in *x*- and *y*-direction. The partial derivatives are then approximated using the finite difference quotient:

$$\frac{\partial \lambda_{nm}}{\partial \Theta} \approx \frac{\lambda_{nm}(\Theta) - \lambda_{nm}(\Theta - h)}{h}. \tag{9}$$

The order of magnitude of the shift h is chosen to be of the same order as the root-mean-square displacement u, which can be calculated since the Debye-Waller factors B are known. For the oxygen atoms in $SrTiO_3$, B equals 0.7323 Å^2 [40, 41], and for the lithium atoms in LiV_2O_4, B equals 1.10 Å^2 [42]. The root-mean-square displacement is then given by [43]:

$$u = \sqrt{\frac{B}{8\pi^2}}. \tag{10}$$

In this case, the value for the shift h in Eq. (9) is set to 0.1562 Å to determine the position of the oxygen column in the crystal $SrTiO_3$, which equals the *x*- and *y*-dimension of the pixel size of the simulated crystal. For a lower value of the shift h, the numerical approximation of the derivative did not improve any further. In the case of locating lithium in the crystal LiV_2O_4 the value for the shift h is analogously set to 0.1648 Å in the *x*-direction and 0.1665 Å in the *y*-direction, corresponding to the *x*- and *y*-dimension of the pixel size of the simulated LiV_2O_4 crystal. Results of the CRLB are presented in Section 5.

3.4. Simulation settings

In the simulations, the Scherzer settings for the spherical aberration and defocus are chosen. The Scherzer defocus is defined by [44]:

$$\varepsilon = -\operatorname{sign}(C_s)\sqrt{|C_s|\lambda}, \tag{11}$$

with λ the electron wavelength and C_s the spherical aberration. It can be shown that minimising the aberration function results in an optimal aperture size α for the probe, given by [45]:

$$\alpha = 1.41\left(\frac{\lambda}{C_s}\right)^{1/4}. \tag{12}$$

By first selecting an experimentally feasible and appropriate semi-convergence angle for the probe, one can thus obtain values for the Scherzer defocus and spherical aberration for a given accelerating voltage. An experimentalist, however, will optimise the defocus by eye and work at a spherical aberration constant of about 1 micron, which is basically the error-bar on the spherical aberration for aberration-corrected microscopes nowadays. The defocus will then typically lie in the range of the Scherzer defocus corresponding to this spherical aberration of 1 micron, which equals -1.4 nm for an acceleration voltage of 300 kV, following Eq. (11). Therefore, the Scherzer defocus corresponding to a spherical aberration of 1 micron and an acceleration voltage of 300 kV are chosen in this work combined with the often used convergence angle of 21.7 mrad in the case of LiV_2O_4, and 20 mrad in the case of $SrTiO_3$.

The influence of the crystal thickness on the optimal experiment design, both for detecting and locating light atoms is investigated. Therefore, simulated STEM images at three different thicknesses are compared. For detecting and locating the pure lithium column in LiV_2O_4 viewed from the [110] direction, the three different thicknesses of 1.17 nm, 2.91 nm and 4.66 nm, corresponding to a column of respectively 2, 5 and 8 Li atoms thick, are compared. For detecting and locating the oxygen column in $SrTiO_3$, the three thicknesses of 1.95 nm, 3.91 nm and 29.29 nm are compared, corresponding to a column of 5, 10 and 75 Sr atoms thick, respectively. All other simulation parameters, given in Table 1 for the LiV_2O_4 crystal and in Table 2 for the $SrTiO_3$ crystal, are kept constant in order to independently investigate

the influence of the crystal thickness. STEM images are then simulated for a whole range of detector angles, and for the different crystal thicknesses.

The optimal experiment design has been investigated with the STEMsim software [28] using absorptive potential multislice simulations. Although frozen lattice simulations are in principle more accurate, only small deviations in the probability of error are found for thicknesses of 23 nm and larger. The probability of error to detect a pure oxygen column in $SrTiO_3$ is compared when using either absorptive potential or frozen lattice simulations. The results of this comparison are presented in Appendix C.

Since we perform a purely theoretical simulation study, it is assumed that the detector is always centered around the optical axis. In practice, however, this may not always be the case. A small displacement away from the optical axis of the detector can have an influence on the accuracy of the measurement [46, 47], which has to be taken into account in image simulations, in the case when one wants to compare directly with the experiment.

The probability of error for a binary hypothesis test was evaluated and minimised in order to obtain the optimal design for the detection of oxygen from a HR STEM image of the crystal $SrTiO_3$, as well as the detection of lithium from a HR STEM image of the crystal LiV_2O_4. Results for the optimal design to detect light atoms are presented in Section 4.

4. Optimal design to detect light atoms

The results of an elaborate simulation study will now be presented. This study has been performed to minimise the probability of error defined in Section 3.1 in order to optimise the inner and outer detector radii of an annular STEM detector to detect light atoms.

4.1. Detecting Li in LiV_2O_4

The probability of error for the detection of the light lithium atomic column in a LiV_2O_4 crystal was computed for a whole range of detector inner and outer angles, for three different crystal thicknesses and an incoming electron dose of 10^5 $e^-/\text{Å}^2$. The parameters used for the simulation of LiV_2O_4, viewed from the [110] direction, are listed in Table 1. The results of the probability of error for the detection of Li in LiV_2O_4 are shown in Fig. 1. In Fig. 1, the optimal inner and outer detector angles to detect the lithium column are determined by the blue region where the probability of error is minimal. From the results shown in Fig. 1, we can see that the same optimal detector range is obtained for the three thicknesses under study. It can also be seen that the probability of error is lower for detecting atomic columns in a thicker sample region, which means that it is becomes easier to detect a lithium column when the sample region becomes thicker, what could be expected. The results of the probability of error show us which area in the detection plane is most sensitive for detecting light elements. From the results shown in Fig. 1, it is clear that the overall optimal detector range for the detection of light elements is the low angle annular dark field (LAADF) STEM regime, where the inner detector radius is slightly larger than the probe semi-convergence angle of 21.7 mrad. Also local optima are found in the annular bright field (ABF) STEM regime, where the inner and outer detector radii are both lying within the illumination cone. This was also suggested elsewhere [26, 42, 48–52].

4.2. Detecting O in $SrTiO_3$

The simulation parameters which are used for $SrTiO_3$ for a spherical aberration-corrected microscope are listed in Table 2. The results for the probability of error using a binary hypothesis test in order to detect oxygen in the crystal $SrTiO_3$ from a HR STEM image are shown in Fig. 2 for three different thicknesses and for an incoming electron dose of 10^4 $e^-/\text{Å}^2$. From the results shown in Fig. 2, it is clear that for thin crystals the optimal detector collection range corresponding to the regime of minimum probability of error is LAADF STEM, which means that the optimal inner detector angle is only slightly larger than the probe semi-convergence angle. There is also a local optimum in the ABF STEM region, where both the inner and outer detector radius are lying within the illumination cone. For thicker crystals, we can see that the optimal region broadens and the optima in the ABF and LAADF STEM regions start to overlap. Moreover, it can be seen that for the thicker crystal, there is a broader range where the probability of error is very low and does not change a lot, which indicates that it becomes less critical to optimise the detector design if one wants to detect an atomic column in a thicker sample region.

5. Optimal design to locate light atoms

In this section, results for the optimal design to locate light atomic columns with the highest precision will be given. This analysis is based on the CRLB, defined in Section 3.2. To calculate this lower bound on the variance of the estimated atomic column position,

Parameter	Symbol	Value
Defocus	ε (nm)	-1.4
Spherical aberration	C_s (mm)	0.001
Slice thickness	z_{slice} (Å)	1.46
Debye-Waller factor Li	B (Å^2)	1.1
Debye-Waller factor V	B (Å^2)	0.01
Debye-Waller factor O	B (Å^2)	0.48
Acceleration voltage	V (kV)	300
Semi-convergence angle	α (mrad)	21.7
Probe sampling distance (x-direction)	Δx (Å)	0.165
Probe sampling distance (y-direction)	Δy (Å)	0.167
Incident electron dose	D (e^-/Å^2)	10^5
FWHM of the source image	$FWHM_s$ (Å)	0.7
Total number of scanned pixels	$N \times M$	50×35

Table 1: Parameter values used in the STEMsim software for the simulation of LiV_2O_4.

a simulation study was performed for both the crystals LiV_2O_4 and $SrTiO_3$ of which the simulation parameters are given in Table 1 and Table 2, respectively. The precision with which the atomic column coordinates can be measured is represented by the diagonal elements of the CRLB. Since both diagonal elements of the CRLB are equivalent for the investigated crystals in this paper, the first one is chosen as optimality criterion, corresponding to the lower bound on the variance of the x-coordinate of the atomic column position. The highest precision to locate a column is then given by the lower bound on the standard deviation of the estimated atomic column position, defined by the square-root of the criterion that is minimised, $\sqrt{\text{CRLB}_{11}}$.

5.1. Locating Li in LiV_2O_4

The ultimate precision with which the position of the pure lithium column in LiV_2O_4 can be determined was calculated for an incoming electron dose of $10^5 e^-/\text{Å}^2$, for a whole range of inner and outer detector angles for the annular STEM detector. This electron dose was chosen in order to retrieve an ultimate precision that lies in the picometre range as desired. The detector settings leading to the minimum value of the $\sqrt{\text{CRLB}_{11}}$ thus result in the ultimate precision to locate the lithium column. Results for this ultimate precision are shown in Fig. 3 for the same thicknesses that were investigated for the detection problem in Section 4.1. From the results shown in Fig. 3, it is clear that the overall optimal detector collection range to locate light atomic columns is LAADF STEM, which was also the optimal detector range for the detection of light elements. Local optima are again found in the ABF STEM regime for the different investigated thicknesses. From Fig. 3 it is also clear that a better precision can be obtained for locating an atomic column in a thicker sample region. This can intuitively be understood since it is easier to determine the position of a column with a higher contrast.

5.2. Locating O in $SrTiO_3$

The ultimate precision with which the position of the pure oxygen column in $SrTiO_3$ can be determined, was calculated for an incoming electron dose of $10^4 e^-/\text{Å}^2$, for a whole range of inner and outer detector angles for the annular STEM detector. A lower dose here suffices in order to obtain picometre precision, since oxygen is a heavier atom and thus gives a higher scattered intensity as compared to lithium. In Fig. 4 it can be seen that the overall optimal detector range is again LAADF STEM, while local optima are present in the ABF STEM regime, at least up to a thickness of 4 nm. For thicker sample regions however, both regimes broaden and start to overlap and the true optimum becomes ABF STEM. From the results shown in Fig. 4, we can also see that a better precision can be obtained when locating an atomic column in a thicker sample region.

In addition to the results shown in Fig. 3 and 4, a line scan is plotted of the attainable precision as a function of thickness at the optimal detector design, to better visualise the attained picometre range precision. These line scans are shown in Fig. 5(a) and 5(b) for the same electron doses that were used in Fig. 3 and 4, respectively. In Fig. 5(a) the ultimate precision to locate the

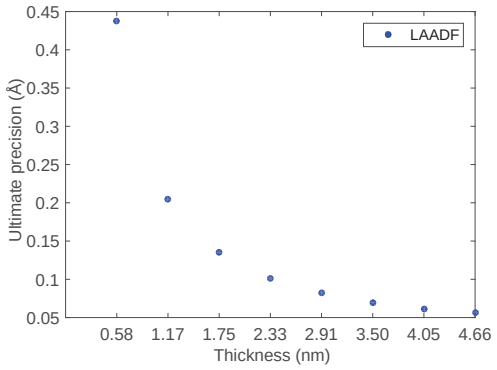

(a) Li column in LiV_2O_4, $D = 10^5 e^-/Å^2$

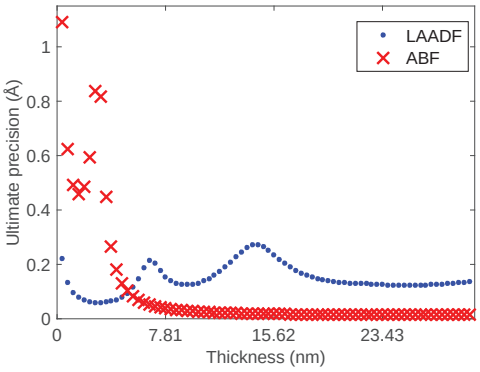

(b) O column in $SrTiO_3$, $D = 10^4 e^-/Å^2$

Figure 5: The ultimate precision to locate a column for an incoming electron dose D as a function of thickness, at the optimal detector settings for detecting and locating the column.

lithium column in LiV_2O_4 is plotted at the obtained optimal detector design, as a function of thickness. In Fig. 5(b) the ultimate precision is plotted to locate the pure O column in $SrTiO_3$ as a function of thickness, at the two optimal settings that were derived for the different considered crystal thicknesses. It can be seen from this figure that from a thickness of 5 nm and larger, the optimal detector setting shifts from LAADF STEM to ABF STEM.

6. Discussion

6.1. Detecting versus locating

Although a single optimum is found for both simulation studies in order to detect and locate light atoms, it can be seen by comparing either Figs. 1 and 3 or Figs. 2 and 4, that the optimal detector region becomes broader in the results of the precision, as compared to the optimal detector region where the probability of error is minimal. This suggests that it is more critical to optimise the experiment design for detecting than for locating light atoms. Therefore, as soon as the experiment design is optimised in order to detect light atomic columns, these columns can also be located with a high precision.

6.2. Dose effect

The detectability of atomic columns as well as the precision to locate them do not only depend on the detector settings, but also on the number of incident electrons. Although the optimal detector settings are independent of the electron dose, the probability of error and the attainable precision can be further analysed as a function of the incident electron dose, both for detecting and locating atomic columns. Especially for light element crystals, the effect of radiation damage is almost unavoidable and therefore one might be interested to investigate the lowest possible incident electron dose, for which the detectability as well as the precision for locating the light atoms are sufficiently high.

From the previous results of the probability of error and the ultimate precision, we obtained a single optimal detector design to both detect and locate a lithium column in LiV_2O_4, as desired. In Fig. 6, results of the probability of error and the ultimate precision as a function of incoming electron dose are shown, both at the respective optimal detector settings for the different thicknesses. From the results shown in Fig. 6(a), it is clear that the probability to choose the wrong hypothesis decreases for an increasing electron dose, as expected. If one finds a maximum probability of error of 10% acceptable, an incident electron dose of about 5500 $e^-/Å^2$ would be sufficient when using the optimal detector settings for detecting Li in LiV_2O_4 for a column of 4.66 nm. From Fig. 6(a), it can also be seen that a higher incoming electron dose is necessary if one wants to detect a lithium column in a very thin sample region with a sufficiently low probability of error. About 7900 incoming electrons per $Å^2$ are therefore necessary to detect a lithium column of 2.91 nm thick, in order to still obtain a maximum probability of error of 15 %.

Also, for locating the lithium columns in LiV_2O_4 one can look at the effect of the electron dose on the attainable precision. Therefore, for the three different thicknesses the ultimate precision is investigated as a function of the electron dose at the optimal detector settings. Results are shown in Fig. 6(b). It can be seen that for an electron dose of $10^5 e^-/Å^2$, the ultimate precision lies in the picometre range as desired when the optimal detector setting for the respective crystal thicknesses is applied. If we compare Figs. 6(a) and 6(b), we propose

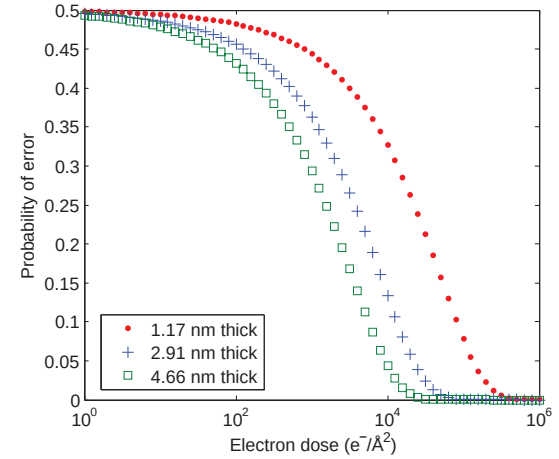

(a) Probability of error

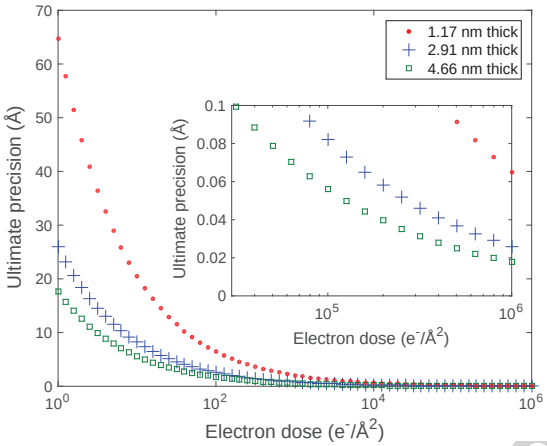

(b) Ultimate precision

Figure 6: (a) The probability of error to detect a Li column in LiV_2O_4 and (b) the ultimate precision to locate a lithium column in LiV_2O_4, both as a function of the electron dose for three different crystal thicknesses: 1.17 nm, 2.91 nm and 4.66 nm at the optimal detector settings for detecting and locating Li.

$10^5 e^-/Å^2$ as optimal incoming electron dose, since at this incoming dose picometre precision for locating the lithium column in LiV_2O_4 is obtained, at least for thicknesses of 2.91 nm or larger, while for the detection of lithium in LiV_2O_4 a very low probability of error of maximum 15% is found, even for a column in a very thin sample region.

Also for the simulation study of $SrTiO_3$ the probability of error and the attainable precision can be investigated as a function of the incident electron dose. In the same way as for the LiV_2O_4 crystal, results are shown in Figs. 7(a) and 7(b) for respectively the probability of error and the ultimate precision as functions of incoming electron dose, under the optimal detector settings for the different investigated crystal thicknesses. For detecting and locating the central O column, the probability of error and the ultimate precision both lead to the same optimal detector range as desired. Both quantities also decrease as a function of the incoming electron dose. From the results shown in Fig. 7, it is clear that a very low probability of error is already obtainable for an incoming dose of about $10^3 e^-/Å^2$. However, a higher dose of $10^4 e^-/Å^2$ is necessary if one also wants to have picometre precision for the oxygen column position in

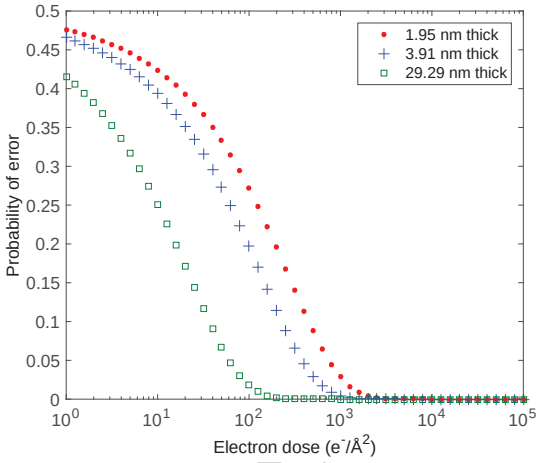

(a) Probability of error

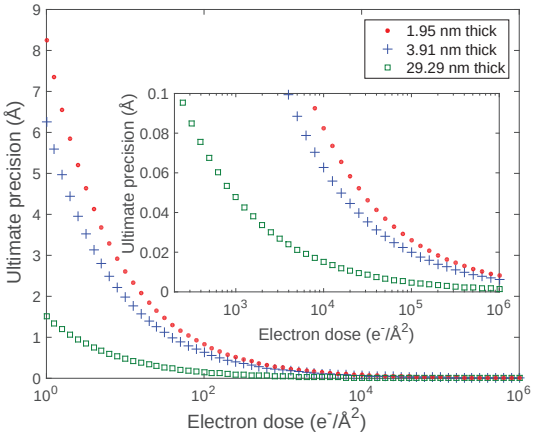

(b) Ultimate precision

Figure 7: (a) The probability of error to detect the central O column in $SrTiO_3$ and (b) the ultimate precision to locate the O column in $SrTiO_3$, both as a function of the electron dose for three different crystal thicknesses: 1.95 nm, 3.91 nm and 29.29 nm at the optimal detector settings for detecting and locating O.

the $SrTiO_3$ crystal.
From these results, it can be shown that one can tune the incoming electron dose in such a way that a sufficiently low probability of error is attained in order to detect a light atomic column, and moreover a high precision on the atomic column position is retrieved. From the results shown in Figs. 6 and 7 it is also clear that the thicker the sample region, the easier it is to detect and locate the atomic column, which is an expected result. Note that in this work, the fundamental counting-statistics limit is established, while in a real experiment the presence of scan noise and other instabilities occur which will make this ideal situation unlikely to be routinely realised.

7. Conclusions

In this paper, the limits to the precision with which light atoms can be detected and located from HR STEM images, are investigated. It is proposed to use statistical detection theory in order to optimise the detector design for the detection problem. To study the optimal design to locate light elements, use is made of the concept of Fisher information. With these statistical tools, the most sensitive regions in the detection plane could be investigated for both research questions, which can be useful for experimentalists when choosing the appropriate camera length for their experiment.
For the detection of light elements from HR STEM images it is found that the thicker the sample region becomes, the easier it will be to detect the light atomic column. The optimal detector design depends on the investigated material and the crystal thickness and corresponds to either ABF STEM, with the detection range lying within the illumination cone of the probe, or LAADF STEM, with an inner detector angle slightly larger than the probe semi-convergence angle. Both optimal regions start to overlap when the sample region becomes thicker.
The optimal settings obtained for locating the light Li and O atoms in the crystals LiV_2O_4 and $SrTiO_3$ are consistent with the optimal settings for the detection of these light atoms in the same crystals. This means that by comparing the detectability with the precision for the locating problem as a function of incoming electron dose, a single optimum is found for which the light element can be detected with a low probability of error and also located with a precision in the picometre range. This optimal incoming electron dose however depends on the crystal structure and thickness. For detecting and locating either Li in LiV_2O_4 or O in $SrTiO_3$ we propose an incoming electron dose of the order of $10^5 e^-/\text{Å}^2$ or $10^4 e^-/\text{Å}^2$ respectively, under the optimal detector settings. Finally, it is also shown for increasing crystal thicknesses that the optimal detector range for the detection of light elements shifts from the LAADF STEM to the ABF STEM regime and the total optimal range also broadens.
In conclusion, the proposed methods can be applied to a wide range of materials applications in order to provide objective suggestions for the inner and outer angle of the annular STEM detector in order to both detect specific atoms with the lowest probability of error, and locate atomic columns with the highest precision. In future work, the present analysis will be extended to include also the effect of strain as this may have an influence on the choice of proposed detector settings [53].

Acknowledgements

The authors acknowledge financial support from the Research Foundation Flanders (FWO, Belgium) through project fundings (G.0368.15, G.0369.15 and G.0374.13) and a postdoctoral research grant to A. De Backer. The research leading to these results has also received funding from the European Union Seventh Framework Programme [FP7/2007-2013] under Grant agreement no. 312483 (ESTEEM2). The authors would also like to thank A. Rosenauer for providing access to the STEMsim software and Gerardo T. Martinez for fruitful discussions.

Appendix A. Binary hypothesis testing

To detect a certain atom type in a STEM image, a binary hypothesis test can be used in which only two possible hypotheses are considered, namely whether the light atom is present or absent. The hypotheses of the binary hypothesis test for the atomic number Z are then given by:

$$\begin{aligned} \mathcal{H}_0 &: \mathrm{Z} = \mathrm{Z}_1 \\ \mathcal{H}_1 &: \mathrm{Z} \in \emptyset \end{aligned} \tag{13}$$

where $\mathcal{H}_0$ is referred to as the null hypothesis and $\mathcal{H}_1$ as the alternative hypothesis describing the absence of an atom of any type. In order to express a prior belief in the likelihood of the hypotheses, we assume that the prior probabilities $P(\mathcal{H}_0)$ and $P(\mathcal{H}_1)$ associated with these hypotheses are known. If both hypotheses are equally likely it is reasonable to assign equal prior probabilities of $1/2$. Following the quantitative method explained in

[26], the goal is now to quantify the probability of assigning the wrong hypothesis. In a so-called Bayesian approach, this probability of error $\mathrm{P_e}$ is defined as:

$$\mathrm{P_e} = P\left(\mathcal{H}_0|\mathcal{H}_1\right) P\left(\mathcal{H}_1\right) + P\left(\mathcal{H}_1|\mathcal{H}_0\right) P\left(\mathcal{H}_0\right) \quad (14)$$

with $P\left(\mathcal{H}_i|\mathcal{H}_j\right)$ the conditional probability of deciding $\mathcal{H}_i$ while $\mathcal{H}_j$ is true. Using criterion (14), the two possible errors are weighted appropriately to yield an overall error measure. Decision rules are now defined such that the probability of error is minimised. It is shown in [25] that one therefore should decide $\mathcal{H}_1$ if

$$\frac{p_{\mathbf{w}}(\mathbf{w};\mathcal{H}_1)}{p_{\mathbf{w}}(\mathbf{w};\mathcal{H}_0)} > \frac{P\left(\mathcal{H}_0\right)}{P\left(\mathcal{H}_1\right)} = \gamma, \quad (15)$$

otherwise $\mathcal{H}_0$ is decided. In this expression, $p_{\mathbf{w}}(\mathbf{w};\mathcal{H}_i)$ is the conditional joint probability function (PF) $p_{\mathbf{w}}(\omega;\mathcal{H}_i)$ assuming $\mathcal{H}_i$ to be true, evaluated at the available observations $\mathbf{w}$. For equal prior probabilities of $1/2$, it is clear that γ in Eq. (15) corresponds to 1. We then decide $\mathcal{H}_1$ if

$$\ln LR(\mathbf{w}) \equiv \ln\left(\frac{p_{\mathbf{w}}(\mathbf{w};\mathcal{H}_1)}{p_{\mathbf{w}}(\mathbf{w};\mathcal{H}_0)}\right) > \ln(1) = 0, \quad (16)$$

otherwise $\mathcal{H}_0$ is decided. This corresponds to choosing the hypothesis for which the log-likelihood function is maximal. The function $LR(\mathbf{w})$ is called the likelihood ratio since it indicates for each set of observations $\mathbf{w}$ the likelihood of $\mathcal{H}_1$ versus the likelihood of $\mathcal{H}_0$. The left-hand side of Eq. (16) is termed the log-likelihood ratio, which can now be used to rewrite the probability of error $\mathrm{P_e}$ defined by Eq. (14), given the decision rule of Eq. (16):

$$\mathrm{P_e} = \frac{1}{2} P\left(\ln LR(\mathbf{w}) < 0|\mathcal{H}_1\right) + \frac{1}{2} P\left(\ln LR(\mathbf{w}) > 0|\mathcal{H}_0\right). \quad (17)$$

Since the pixel values in a STEM image are assumed to be independent, the probability that a set of observations equals $\{\omega_{nm}|n = 1, ..., N; m = 1, ..., M\}$ is the product of all probabilities given by Eq. (1):

$$p_{\mathbf{w}}(\omega;\mathcal{H}_i) = \prod_{n=1}^{N}\prod_{m=1}^{M} \frac{\lambda_{nm}^{\omega_{nm}}}{\omega_{nm}!} \exp\left(-\lambda_{nm}\right) \quad (18)$$

Using this conditional joint PF, the log-likelihood ratio defined by Eq. (16) can be rewritten as

$$\ln LR(\mathbf{w}) = \sum_{n=1}^{N}\sum_{m=1}^{M} \mathbf{w}_{nm} \ln\left(\frac{\lambda_{\mathcal{H}_1,nm}}{\lambda_{\mathcal{H}_0,nm}}\right) - \lambda_{\mathcal{H}_1,nm} + \lambda_{\mathcal{H}_0,nm}. \quad (19)$$

Following the central limit theorem, the log-likelihood ratio tends to be normally distributed. For STEM images the expected value μ and variance σ^2 characterising this normal distribution of $\ln LR(\omega)$, can be computed from Eq. (19) when assuming $\mathcal{H}_i$ to be true, giving the following results:

$$\mu_{\mathcal{H}_i} = \sum_{n=1}^{N}\sum_{m=1}^{M} \lambda_{\mathcal{H}_i,nm} \ln\frac{\lambda_{\mathcal{H}_1,nm}}{\lambda_{\mathcal{H}_0,nm}} - \lambda_{\mathcal{H}_1,nm} + \lambda_{\mathcal{H}_0,nm}, \quad (20)$$

$$\sigma_{\mathcal{H}_i}{}^2 = \sum_{n=1}^{N}\sum_{m=1}^{M} \lambda_{\mathcal{H}_i,nm} \left(\ln\frac{\lambda_{\mathcal{H}_1,nm}}{\lambda_{\mathcal{H}_0,nm}}\right)^2. \quad (21)$$

In this derivation, use is made of the property that the variance of a Poisson distributed variable equals its expectation value. The explicit description of the distribution of the log-likelihood ratio now enables us to unambiguously compute the probability of error given by Eq. (17), resulting in the following general expression:

$$\mathrm{P_e} = \frac{1}{2}\left[\Phi\left(\frac{-\mu_{\mathcal{H}_1}}{\sigma_{\mathcal{H}_1}}\right) + \Phi\left(\frac{\mu_{\mathcal{H}_0}}{\sigma_{\mathcal{H}_0}}\right)\right] \quad (22)$$

with $\Phi(\cdot)$ the cumulative distribution function of the standard normal distribution.

Appendix B. The Cramér-Rao Lower Bound

It is proven that for the class of unbiased estimators, the ultimate precision is given by a lower bound on their variance, the CRLB [33–36]. Consider $p_{\mathbf{w}}(\omega;\Theta)$, the joint probability (density) function of a set of observations $\mathbf{w} = (w_{11}, \ldots, w_{NM})^T$. An example of this function is given by Eq. (18) for the pixel intensities in a STEM image. The so-called *Fisher information matrix* measuring the amount of information that an observable random variable carries about an unknown parameter vector $\mathbf{\Theta} \in \mathbb{R}^R$, can then be defined as follows:

$$F = -\mathbb{E}\left[\frac{\partial^2 \ln p_{\mathbf{w}}\left(\omega;\mathbf{\Theta}\right)}{\partial\mathbf{\Theta}\,\partial\mathbf{\Theta}^T}\right], \quad (23)$$

which is an $R\times R$ matrix. The expression between square brackets gives the Hessian matrix of the logarithm of the joint probability (density) function of which the (r, s)th element is given by $\partial^2 \ln p_{\mathbf{w}}(\omega;\mathbf{\Theta})/\partial\Theta_r\partial\Theta_s$. The Fisher information represents the expected value of the observed information and is defined as the variance of the so-called score function, i.e. the derivative of the log-likelihood function with respect to the unknown parameters. Use of the concept of Fisher information allows

one to determine the highest precision, that is, the lowest variance, with which a parameter can be estimated unbiasedly. Suppose that $\widehat{\mathbf{\Theta}}$ is any unbiased estimator of $\mathbf{\Theta}$, that is, $\mathbb{E}[\widehat{\mathbf{\Theta}}] = \mathbf{\Theta}$. Then it can be shown [32] that under general conditions the covariance matrix $\mathrm{cov}(\widehat{\mathbf{\Theta}})$ of $\widehat{\mathbf{\Theta}}$ satisfies

$$\mathrm{cov}\left(\widehat{\mathbf{\Theta}}\right) \geq F^{-1}, \tag{24}$$

so that $\mathrm{cov}(\widehat{\mathbf{\Theta}}) - F^{-1}$ is positive semi-definite and consequently its diagonal elements cannot be negative. This means that the diagonal elements of $\mathrm{cov}\left(\widehat{\mathbf{\Theta}}\right)$, that is, the actual variances of $\widehat{\Theta}_1, ..., \widehat{\Theta}_R$ are larger than or equal to the corresponding diagonal elements of F^{-1}:

$$\mathrm{var}(\widehat{\Theta}_r) \geq \left[F^{-1}\right]_{rr}, \tag{25}$$

where $r \in \{1, ..., R\}$, with R the number of components of $\widehat{\mathbf{\Theta}}$ and $[F^{-1}]_{rr}$ the rth diagonal element of the inverse of the Fisher information matrix. In this sense, F^{-1} represents a lower bound for the variances of all unbiased estimators $\widehat{\mathbf{\Theta}}$. The matrix F^{-1} is the CRLB on the variance of $\widehat{\mathbf{\Theta}}$. It can be shown that there exists an estimator that achieves the CRLB at least asymptotically, that is, for an increasing number of observations. This estimator is the Maximum Likelihood (ML) estimator [8]. In electron microscopy, the number of observations is usually sufficiently large for the asymptotic properties of the ML estimator to apply and the use of this estimator is therefore highly recommended in quantitative electron microscopy [6].

If we consider the position parameter vector $\mathbf{\Theta}$ and the joint Poisson probability function for the pixel intensities in a STEM image given by Eq. (18), it can be shown that Eq. (23) for the Fisher information matrix reduces to:

$$F_{rs} = \sum_n \sum_m \frac{1}{\lambda_{nm}} \frac{\partial \lambda_{nm}}{\partial \Theta_r} \frac{\partial \lambda_{nm}}{\partial \Theta_s}, \tag{26}$$

where the parameter $\lambda_{nm} = I_{nm} \cdot D \cdot \Delta x \Delta y$ corresponds to the expectation values for the pixel intensities of the STEM image, with D the incoming electron dose per Å^2, Δx and Δy the x- and y-dimension of the pixel size, and I_{nm} the expectation values for the pixel intensities of the STEM image for one incoming electron per pixel.

Appendix C. Comparison between absorptive potential and frozen lattice simulations

Absorptive potential simulations are compared with frozen lattice simulations, for the detection of the pure O column in $SrTiO_3$ as a function of thickness. The probability of error at the optimal detector settings that were obtained for the investigated crystal thicknesses using absorptive potential simulations are compared with the result when using frozen lattice simulations, both for ABF and LAADF STEM and for an incoming electron dose of $10^4 e^-/$Å^2. Only small differences in probability of error are found for both simulation methods. The probability of error only differs for both simulation methods in the LAADF STEM regime from a thickness of about 23 nm and larger. It is expected for the thicknesses considered in this paper that the optimal detector design would be the same when performing frozen lattice simulations to optimise the whole detector region.

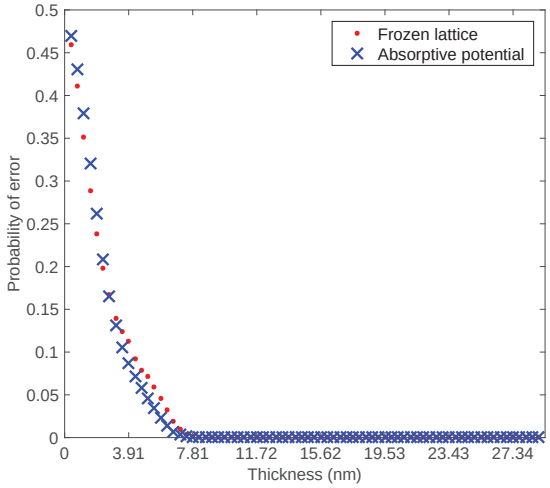

(a) ABF STEM (10-16 mrad)

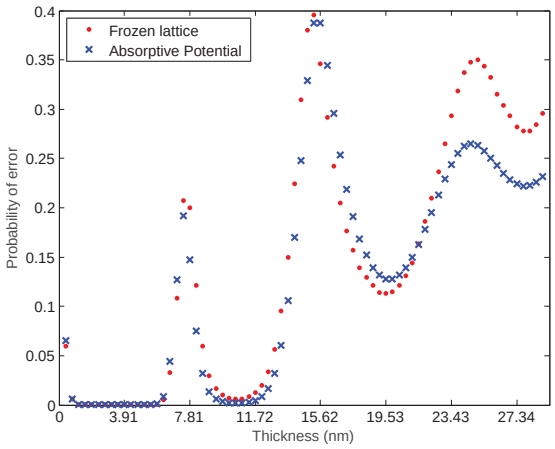

(b) LAADF STEM (21.7-100 mrad)

Figure 8: The probability of error to detect the central O column in $SrTiO_3$ for two different detector settings as a function of crystal thickness and for $D = 10^4 e^-/$Å^2. The frozen lattice result is the average over 100 different lattice configurations.

References

[1] S. Van Aert, A. J. den Dekker, D. Van Dyck, A. van den Bos, Optimal experimental design of STEM measurement of atom column positions, Ultramicroscopy 90 (4) (2002) 273–289.

[2] H. Sawada, Y. Tanishori, N. Ohashi, T. Tomita, F. Hosokawa, T. Kaneyama, Y. Kondo, K. Takayanagi, STEM imaging of 47-pm separated atomic columns by a spherical aberration-corrected electron microscope with a 300-kV cold field emission gun, Journal of Electron Microscopy 58 (2009) 357–361.

[3] X. Sang, J. M. LeBeau, Revolving scanning transmission electron microscopy: Correcting sample drift distortion without prior knowledge, Ultramicroscopy 138 (2013) 28–35.

[4] A. J. den Dekker, S. Van Aert, D. Van Dyck, A. van den Bos, P. Geuens, Does a monochromator improve the precision in quantitative HRTEM?, Ultramicroscopy 89 (2001) 275–290.

[5] D. Van Dyck, S. Van Aert, A. J. den Dekker, A. van den Bos, Is atomic resolution transmission electron microscopy able to resolve and refine amorphous structures?, Ultramicroscopy 98 (2003) 27–42.

[6] A. J. den Dekker, S. Van Aert, D. Van Dyck, A. van den Bos, Maximum likelihood estimation of structure parameters from high resolution electron microscopy image. Part I: A theoretical framework, Ultramicroscopy 104 (2) (2005) 83–106.

[7] S. Van Aert, A. J. den Dekker, A. van den Bos, D. Van Dyck, J. H. Chen, Maximum likelihood estimation of structure parameters from high resolution electron microscopy images: Part II: A practical example, Ultramicroscopy 104 (2005) 107–125.

[8] A. J. den Dekker, J. Gonnissen, A. De Backer, J. Sijbers, S. Van Aert, Estimation of unknown structure parameters from high-resolution STEM images: What are the limits?, Ultramicroscopy 134 (2013) 34–43.

[9] S. J. Pennycook, L. A. Boatner, Chemically sensitive structure-imaging with a scanning transmission electron microscope, Nature 336 (1988) 565–567.

[10] P. Hartel, D. Rose, C. Dinges, Conditions and reasons for incoherent imaging in STEM, Ultramicroscopy 63 (1996) 63–114.

[11] A. Singhal, J. C. Yang, J. M. Gibson, STEM-based mass spectroscopy of supported Re clusters, Ultramicroscopy 67 (1997) 191–206.

[12] P. Voyles, D. A. Muller, J. L. Grazul, P. H. Citrin, H.-J. L. Gossmann, Atomic-scale imaging of individual dopant atoms and clusters in highly n-type bulk Si, Nature 416 (2002) 826–829.

[13] R. Erni, H. Heinrich, G. Kostorz, Quantitative characterisation of chemical inhomogeneities in Al-Ag using high-resolution Z-contrast STEM, Ultramicroscopy 94 (2003) 125–133.

[14] J. M. LeBeau, S. D. Findlay, L. J. Allen, S. Stemmer, Standardless atom counting in scanning transmission electron microscopy, Nano Letters 10 (2010) 4405–4408.

[15] K. Kimoto, T. Asaka, X. Yu, T. Nagai, Y. Matsui, K. Ishizuka, Local crystal structure analysis with several picometer precision using scanning transmission electron microscopy, Ultramicroscopy 110 (2010) 778782.

[16] S. Van Aert, K. J. Batenburg, M. D. Rossell, R. Erni, G. Van Tendeloo, Three-dimensional atomic imaging of crystalline nanoparticles, Nature 470 (2011) 374–377.

[17] S. Bals, M. Casavola, M. A. van Huis, S. Van Aert, K. J. Batenburg, G. Van Tendeloo, D. Vanmaekelbergh, Three-dimensional atomic imaging of colloidal core-shell nanocrystals, Nano Letters 11 (8) (2011) 3420–3424.

[18] S. Bals, S. Van Aert, C. P. Romero, K. Lauwaet, M. J. Van Bael, B. Schoeters, B. Partoens, E. Yücelen, P. Lievens, G. Van Tendeloo, Atomic scale dynamics of ultrasmall germanium clusters, Nature Communications 3 (2012) 897.

[19] S. Van Aert, A. De Backer, G. T. Martinez, B. Goris, S. Bals, G. Van Tendeloo, A. Rosenauer, Procedure to count atoms with trustworthy single-atom sensitivity, Physical Review B 87 (2013) 064107.

[20] A. B. Yankovich, B. Berkels, W. Dahmen, P. Binev, S. I. Sanchez, S. A. Bradley, A. Li, I. Szlufarska, P. M. Voyles, Picometre-precision analysis of scanning transmission electron microscopy images of platinum nanocatalysts, Nature Communications 5 (2014) 4155.

[21] L. Jones, H. Yang, T. Pennycook, M. Marshall, S. Van Aert, N. Browning, M. Castell, P. D. Nellist, Smart align a new tool for robust non-rigid registration of scanning microscope data, Advanced Structural and Chemical Imaging 1 (2015) 8–23.

[22] N. H. Dekkers, H. D. Lang, Differential phase contrast in a STEM, Optik 41 (1974) 452–456.

[23] H. Rose, Image-formation by inelastically scattered electrons in electron-microscopy, Optik 45 (1976) 139158.

[24] H. Yang, T. J. Pennycook, P. D. Nellist, Efficient phase contrast imaging in STEM using a pixelated detector. Part II: Optimisation of imaging conditions, Ultramicroscopy 151 (2015) 232–239.

[25] S. M. Kay, Fundamentals of Statistical Signal Processing. Volume II Detection Theory, Prentice-Hall, Inc., New Jersey, 2009.

[26] J. Gonnissen, A. De Backer, A. J. den Dekker, G. T. Martinez, A. Rosenauer, J. Sijbers, S. Van Aert, Optimal experimental design for the detection of light atoms from high-resolution scanning transmission electron microscopy images, Applied Physics Letters 105 (063116).

[27] J. M. LeBeau, S. D. Findlay, L. J. Allen, S. Stemmer, Quantitative atomic resolution scanning transmission electron microscopy, Physical Review Letters 100 (2008) 206101.

[28] A. Rosenauer, M. Schowalter, Stemsim - a new software tool for simulation of STEM HAADF Z-contrast imaging, in: A. G. Cullis, P. A. Midgley (Eds.), Microscopy of Semiconducting Materials 2007, Vol. 120 of Springer Proceedings in Physics, Springer Netherlands, 2008, pp. 170–172.

[29] A. Rosenauer, K. Gries, K. Müller, A. Pretorius, M. Schowalter, A. Avramescu, K. Engl, S. Lutgen, Measurement of specimen thickness and composition in $Al_xGa_{1-x}N$/GaN using high-angle annular dark field images, Ultramicroscopy 109 (2009) 1171–1182.

[30] T. Grieb, K. Müller, O. Rubel, R. Fritz, C. Gloistein, M. Schowalter, N. Neugebohrn, N. Knaub, K. Volz, A. Rosenauer, Determination of the chemical composition of GaNAs using STEM HAADF imaging and STEM strain state analysis, Ultramicroscopy 117 (2012) 15–23.

[31] L. J. Allen, A. J. D'Alfonso, S. D. Findlay, Modelling the inelastic scattering of fast electrons, Ultramicroscopy 151 (2015) 11–22.

[32] A. van den Bos, Parameter estimation, in: Handbook of Measurement Science. Vol. 1, Wiley, Chisester, 1982.

[33] B. Frieden, Physics from Fisher Information- A Unification, Cambridge University Press, Cambridge, United Kingdom, 1998.

[34] A. van den Bos, A. J. den Dekker, Resolution reconsidered - conventional approaches and an alternative, in: P.W. Hawkes (Ed.), Advances in Imaging and Electron Physics, Vol. 117, Academic Press, San Diego, 2001.

[35] A. Stuart, K. Ord, Kendall's Advanced Theory of Statistics, Arnold, London, 1994.

[36] R. Jennrich, An Introduction to Computational Statistics - Regression Analysis, Prentice Hall, Englewood Cliffs, NJ, 1995.

[37] S. Van Aert, A. J. den Dekker, D. Van Dyck, A. van den Bos, High-resolution electron microscopy and electron tomography: resolution versus precision, Journal of Structual Biology 138 (2002) 21–33.

[38] S. Van Aert, A. J. den Dekker, A. van den Bos, D. Van Dyck, High-resolution electron microscopy: From imaging toward measuring, IEEE Transactions on Instrumentation and Measurement 51 (4) (2002) 611–615.
[39] A. Mood, F. Graybill, D. Boes, Introduction to the Theory of Statistics, 3rd Edition, McGraw-Hill, Tokyo, 1974.
[40] Y. A. Abramov, V. G. Tsirelson, The chemical bond and atomic displacements in $SrTiO_3$ from X-ray diffraction analysis, Acta Crystallography B 51 (1995) 942–951.
[41] L.-M. Peng, Anisotropic thermal vibrations and dynamical electron diffraction by crystals, Acta Crystallography A 53 (1997) 663–672.
[42] S. Lee, Y. Oshima, H. Sawada, F. Hosokawa, E. Okunishi, Counting lithium ions in the diffusion channel of an LiV_2O_4 crystal, Journal of Applied Physics 109 (113530).
[43] R. A. Blessing, D. Y. Guo, D. A. Langs, Statistical expectation value of the Debye-Waller factor and $e(hkl)$ values for macromolecular crystals, Acta Crystallography D 52 (1996) 257–266.
[44] O. Scherzer, The theoretical resolution limit of the electron microscope, Journal of Applied Physics 20 (1949) 20–29.
[45] M. D. Weyland, D. A. Muller, Tuning the convergence angle for optimum STEM performance, FEI Nanosolutions 1 (2005) 24–35.
[46] S. D. Findlay, J. M. LeBeau, Detector non-uniformity in scanning transmission electron microscopy, Ultramicroscopy 124 (2013) 52–60.
[47] F. F. Krause, M. Schowalter, T. Grieb, K. Müller-Caspary, T. Mehrtens, A. Rosenauer, Effects of instrument imperfections on quantitative scanning transmission electron microscopy, Ultramicroscopy 161 (2016) 146–160.
[48] S. D. Findlay, N. R. Lugg, N. Shibata, L. J. Allen, Y. Ikuhara, Prospects for lithium imaging using annular bright field scanning transmission electron microscopy: A theoretical study, Ultramicroscopy 111 (2011) 1144–1154.
[49] Y. Oshima, H. Sawada, F. Hosokawa, E. Okunishi, T. Kaneyama, Y. Kondo, S. Niitaka, H. Takagi, Y. Tanishiro, K. Takayanagi, Direct imaging of lithium atoms in LiV_2O_4 by spherical aberration-corrected electron micrscopy, Journal of Electron Microscopy 59 (2010) 457–461.
[50] E. Okunishi, I. Ishikawa, H. S. F. Hosokawa, M. Hori, Y. Kondo, Visualization of light elements at ultrahigh resolution by STEM annular bright field microscopy, Microscopy and Microanalysis 15 (2009) 164–165.
[51] S. D. Findlay, N. Shibata, H. Sawada, E. Okunishi, Y. Kondo, Y. Ikuhara, Dynamics of annular bright field imaging in scanning transmission electron microscopy, Ultramicroscopy 110 (2010) 903–923.
[52] R. Ishikawa, E. Okunishi, H. Sawada, Y. Kondo, F. Hosokawa, E. Abe, Direct imaging of hydrogen-atom columns in a crystal by annular bright-field electron microscopy, Nature Materials 10 (2011) 278–281.
[53] V. Grillo, K. Mueller, K. Volz, F. Glas, T. Grieb, A. Rosenauer, Strain, composition and disorder in ADF imaging of semiconductors, Journal of Physics: Conference Series 326 (2011) 012006.

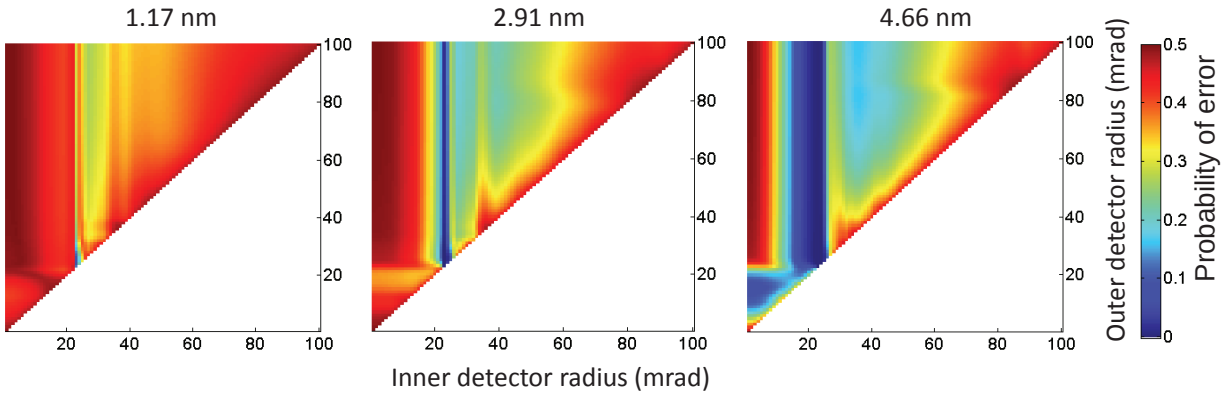

Figure 1: The probability of error to detect Li in a 1.17 nm, 2.91 nm and 4.66 nm thick LiV_2O_4 crystal respectively using a binary hypothesis test, for an incoming electron dose of 10^5 $e^-/Å^2$. On the horizontal axes, the inner detector radius is shown and on the vertical axes the outer detector radius, both in mrad.

Parameter	Symbol	Value
Defocus	ε (nm)	-1.4
Spherical aberration	C_s (mm)	0.001
Slice thickness	z_{slice} (Å)	1.95
Debye-Waller factor Sr	B (Å^2)	0.6214
Debye-Waller factor Ti	B (Å^2)	0.4398
Debye-Waller factor O	B (Å^2)	0.7323
Acceleration voltage	V (kV)	300
Semi-convergence angle	α (mrad)	20
Probe sampling distance (x- and y-direction)	Δx, Δy (Å)	0.075
Incident electron dose	D ($e^-/Å^2$)	10^4
FWHM of the source image	$FWHM$ (Å)	0.7
Number of scanned pixels for detecting O	$N \times M$	52×52
Number of scanned pixels for positioning O	$N \times M$	25×25

Table 2: Parameter values used in the STEMsim software for the simulation of $SrTiO_3$.

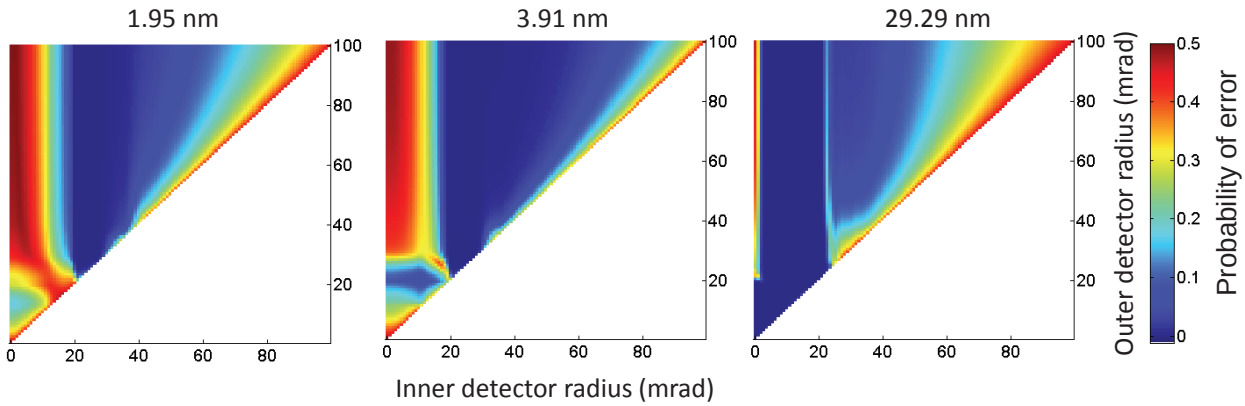

Figure 2: The probability of error to detect O in a 1.95 nm, 3.91 nm and 29.29 nm thick $SrTiO_3$ crystal using a binary hypothesis test, for an incoming electron dose of $10^4\ e^-/\text{Å}^2$. On the horizontal axes, the inner detector radius is shown and on the vertical axes the outer detector radius, both in mrad.

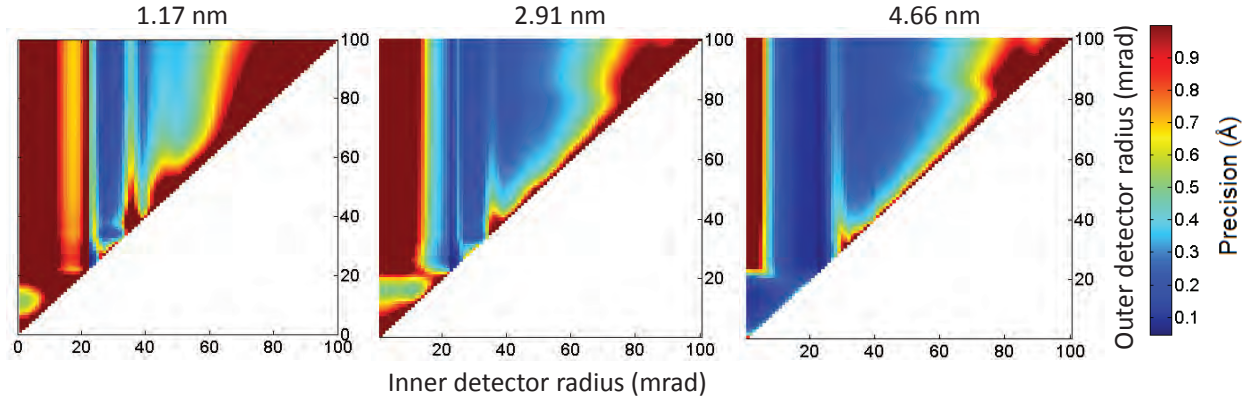

Figure 3: The precision with which the pure Li column can be located in LiV_2O_4 using a binary hypothesis test for the three different crystal thicknesses of 1.17 nm, 2.91 nm and 4.66 nm respectively and the same incoming electron dose of $10^5 e^-/\text{Å}^2$. On the horizontal axes, the inner detector radius is shown and on the vertical axes the outer detector radius, both in mrad. Note that the maximum value of the colorbar is set to 1 in order to visualise the optimal region.

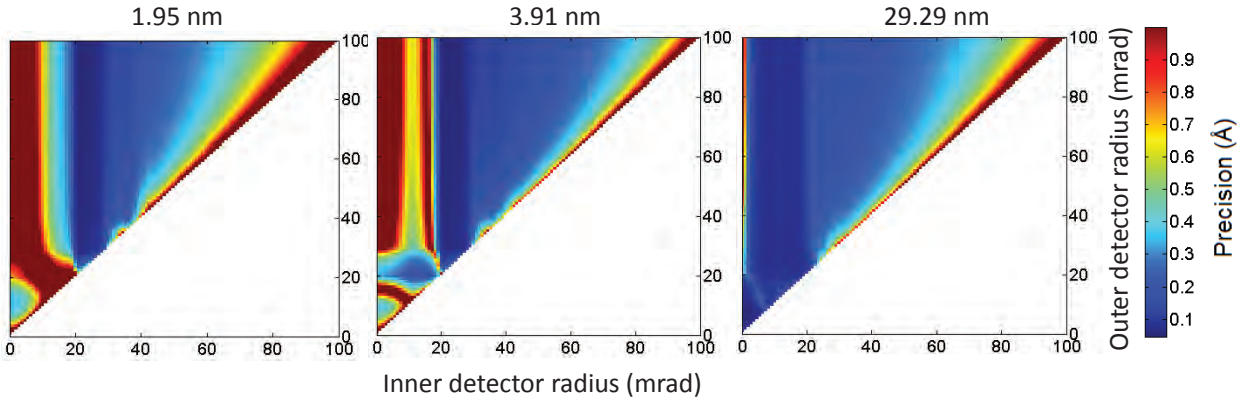

Figure 4: The precision with which the pure O column can be located in $SrTiO_3$ using a binary hypothesis test for the three different crystal thicknesses 1.95 nm, 3.91 nm and 29.29 nm respectively and the same incoming electron dose of $10^4 e^-/Å^2$. On the horizontal axes, the inner detector radius is shown and on the vertical axes the outer detector radius, both in mrad. Note that the maximum value of the colorbar is set to 1 in order to visualise the optimal region.